MULTIPLE MULTIPOLE EXPANSIONS FOR ELASTIC SCATTERING: AN AID TO UNDERSTANDING THE PROBLEMS IN "NO-RECORD" AREAS

Matthias G. Imhof

Earth Resources Laboratory
Department of Earth, Atmospheric, and Planetary Sciences
Massachusetts Institute of Technology
Cambridge, MA 02139

ABSTRACT

This paper presents a new approach to solving scattering of elastic waves in two dimensions. Wavefields are often expanded into an orthogonal set of basis functions. Unfortunately, these expansions converge rather slowly for complex geometries. The new approach enhances convergence by summing multiple expansions with different centers of expansion. This allows irregularities of the boundary to be resolved locally from a nearby center of expansion. Mathematically, the wavefields are expanded into a set of non-orthogonal basis functions. The incident wavefield and the fields induced by the scatterers are matched by evaluating the boundary conditions at discrete matching points along the domain boundaries. Due to the non-orthogonal expansions, more matching points are used than actually needed, resulting in an overdetermined system which is solved in the least squares sense.

Since there are free parameters such as the location and number of expansion centers as well as the kind and orders of expansion functions used, numerical experiments are performed to measure the performance of different discretizations. An empirical set of rules governing the choice of these parameters is found from these experiments. The resulting algorithm is a general tool to solve relatively large and complex two-dimensional scattering problems.

INTRODUCTION

In many areas of the world, the nature of the local geology hinders reflection seismic exploration. Commonly, it is the presence of high-velocity layers in the near-subsurface

which makes it difficult to image deeper reflectors. Examples of such geologies are layers of basalt, carbonates or permafrost. The P-wave penetration problem often seems to occur when these high velocity layers are juxtaposed against much lower velocity materials. Reflections from depth are almost impossible to interpret on surface seismic data acquired in this region. One reason is due to strong reverberations from energy trapped in zones of lower velocity (Pujol *et al.*, 1989). These reverberations may mask any deeper reflections present in the data. Also, the waves transmitted through the high velocity layer are subject to attenuation by wave absorption or by scattering at heterogeneities (Wu and Aki, 1985). In addition to the P-wave problem, source-generated noises such as surface waves, are strongly scattered, delayed by variable amounts and rendered uncoherent. All this noise clouds the reflections sought even more (Pritchett, 1990). Mode conversion of both reflected and transmitted waves also becomes very efficient in all these situations. Pujol (1989) and Papworth (1985) associated strong S-wave arrivals with P-S conversion at basalt surfaces encountered in land surveys. Finally, in the near-subsurface or within waveguides such as the low velocity layer, body waves convert to surface waves and vice versa. All these different mechanisms render the wavefields less coherent, generate additional 'noise' and amplify source-generated noise effects.

Conoco, Inc. provided a data set acquired in West Texas over high-velocity carbonate formations. As examples, two shot gathers are shown in Figures 1 and 2. Both records are badly contaminated by 'noise'. The data processors found many problems associated with backscattered Rayleigh waves. In this paper, we propose a numerical scheme to study the effect of heterogeneities.

Various methods have been proposed assuming the medium consists of homogeneous regions with sharp boundaries in between. Then, reflectivity (Müller, 1985; Kennett, 1983) and global matrix methods (Chin *et al.*, 1984) are routinely used for planarly or cylindrically layered media. For laterally heterogeneous media, numerical integration over wavenumber can be used (Bouchon and Aki, 1977; Haartsen *et al.*, 1994).

The classical eigenfunction expansion (SMP) (Morse and Feshbach, 1953) allows the analysis of simple shapes only, such as circular or elliptical cylinders, where the eigenfunctions are known (Bowman *et al.*, 1969; Pao and Mow, 1973). Methods based on the perturbation of a prescribed geometry, such as the T-matrix method (Waterman, 1976; Boström, 1980) work extremely well for certain geometries but are harder to apply efficiently in general situations such as slender scattering objects (Lakhtakia *et al.*, 1984).

The method we present is a derivative of boundary element methods (BEM) (Brebbia and Dominguez, 1989). It was first presented as a more general approach for electromagnetic scattering (Ballisti and Hafner, 1983; Hafner, 1990) and later adapted to acoustic scattering problems (Imhof, 1995a). In contrast to more traditional approaches, the wavefields are expanded into a set of *non-orthogonal* and *non-complete* basis functions. Actually, non-complete basis functions are not a new concept since, for numerical and computational reasons, we can never use an infinite number of basis functions. But, the simultaneous use of a non-orthogonal expansion allows us to reduce truncation errors

(Hafner, 1993).

To solve for the unknown weighting coefficients of the basis functions, discrete matching points are chosen along the boundary of the scattering object. In the elastic case, each matching point provides four boundary conditions and thus four equations involving the unknowns. Because the expansion is non-orthogonal, we need more equations than unknowns, thus building an overdetermined matrix system and solving it in the *least-squares sense*. Mathematically speaking, we search for the set of weighting coefficients which solves the problem at hand "best" employing the expansions chosen. In fact, we build a model for the wavefields and invert for the "optimal" set of parameters. There will always be an error in the boundary conditions at each matching point, although on average these errors are small. Furthermore, the fields in between matching points are forced to be smooth, such that no wild jumps or oscillations can occur. Thus, as an added bonus, we control the behavior of the expansions in between matching points where we have no control using traditional methods. Also, this allows us to see in which parts of the boundary the chosen expansions can solve the problem and where they need further refinement.

The method is well-suited for solving scattering from either one scatterer alone or between multiple scatterers. Each scatterer consists of a homogeneous and bounded region embedded in a homogeneous and unbounded background. Applications of the problems posed can be found in geophysical exploration or earthquake engineering, ultrasonic nondestructive testing and medial imaging or underwater acoustics. The computer runtime and the memory requirements are functions of the interface area of the embedded scatterers. Due to its close relationship with other matrix methods such as finite elements, a hybridized scheme (Imhof, 1995b) can be devised easily, which allows one to embed heterogeneous scatterers in a homogeneous background.

This paper is structured as follows: First, we adapt the method from acoustical (Imhof, 1995a) to elastic scattering. Then we present results from several calculations and compare them to solutions obtained by the finite difference method and the classical eigenfunction expansion. We show how different discretizations affect the resulting solutions. Finally, we compile these findings into an empirical set of rules which allows us to set up a problem in a fashion which yields satisfactory results without having to resort to a trial and error approach.

THEORETICAL BACKGROUND

We model how an incident wavefield $\mathbf{u}^{inc}(\mathbf{x},\omega)e^{i\omega t}$ scatters from an object. The situation is depicted in Figure 3. For simplicity sake, we will suppress the harmonic time factor $e^{i\omega t}$ in all the following expressions. Superscripts will denote the region to which a material property or field belongs to, and, to distinguish different regions or domains, we will use the symbol Γ^d. The boundary between the two regions Γ^0 and Γ^1 will be denoted by $\partial\Gamma_{01}$. Also, the homogeneous and unbounded region Γ^0 will often be called the 'background'. All other regions Γ^d where $d \neq 0$ are homogeneous, but bounded.

They will be called 'scatterers'.

In the frequency domain, the displacement $\mathbf{u}(\underset{\sim}{\mathbf{x}}, \omega)$ of an elastic P-SV wave travelling in a two-dimensional, homogeneous medium is described by (Pao and Mow, 1973)

$$\frac{1}{k^2}\nabla\nabla\cdot\mathbf{u} - \frac{1}{l^2}\nabla\times\nabla\times\mathbf{u} + \mathbf{u} = 0 \tag{1}$$

where we defined the wave vectors $k = \omega/\alpha$ and $l = \omega/\beta$ for a particular frequency ω and the propagation velocities $\alpha = \sqrt{\lambda + 2\mu/\rho}$ and $\beta = \sqrt{\mu/\rho}$. The parameters ρ, λ and μ denote the density and the Lamé parameters of the medium, respectively.

In a local cylindrical coordinate system (r, θ, y) centered at a point $\mathbf{x}_p$ (Figure 4), the strains due to a displacement $\mathbf{u}$ are expressed as (Pao and Mow, 1973)

$$\epsilon_{rr} = \frac{\partial u_r}{\partial r} \tag{2a}$$

$$\epsilon_{\theta\theta} = \frac{\partial u_\theta}{\partial \theta} + \frac{\partial u_r}{\partial r} \tag{2b}$$

$$\epsilon_{r\theta} = \epsilon_{\theta r} = \frac{1}{2}\left(\frac{1}{r}\frac{\partial u_r}{\partial \theta} + \frac{\partial u_\theta}{\partial r} - \frac{u_\theta}{r}\right). \tag{2c}$$

All other components are zero since they involve the u_y component or cross-derivatives with respect to y. The stresses are linearly related to the strains by (Pao and Mow, 1973)

$$\sigma_{pq} = \lambda\delta_{pq}\sum_k \epsilon_{kk} + 2\mu\epsilon_{pq} \qquad \text{where} \qquad p, q \in \{r, \theta\}. \tag{3}$$

A displacement field $\mathbf{u}^{inc}(\mathbf{x})$ incident on the scatterer will induce two scattered fields: $\mathbf{u}^0(\mathbf{x}, \omega)$ outside the scattering object and $\mathbf{u}^1(\mathbf{x}, \omega)$ on the inside. The displacements and stresses inside and outside the scatterer are related by the boundary conditions. For the problem posed, these conditions are continuity of displacement and stresses in both normal and tangential directions. We define the normal $\hat{\mathbf{n}}$ to point from medium Γ^0 into medium Γ^1, as depicted in Figure 4. Using the subscripts n and t to denote the normal and tangential direction, we write

$$u_n^0 + u_n^{inc} = u_n^1 \tag{4a}$$

$$u_t^0 + u_t^{inc} = u_t^1 \tag{4b}$$

$$\sigma_{nn}^0 + \sigma_{nn}^{inc} = \sigma_{nn}^1 \tag{4c}$$

$$\sigma_{nt}^0 + \sigma_{nt}^{inc} = \sigma_{nt}^1 \tag{4d}$$

Since we express the displacements and stresses in a local cylindrical coordinate system (r, θ, y), but want to specify the boundary in a local cartesian system (n, t, y), we have to use the rotation matrix $\mathbf{M}$ to transform the individual components

$$\mathbf{u}_{nty} = \mathbf{M}\cdot\mathbf{u}_{r\theta y} \tag{5}$$

$$\boldsymbol{\sigma}_{nty} = \mathbf{M}\cdot\boldsymbol{\sigma}_{r\theta y}\cdot\mathbf{M}^T \tag{6}$$

where the rotation matrix M is defined by the unit vectors $\hat{\mathrm{r}}$, $\hat{\theta}$, $\hat{\mathrm{n}}$ and $\hat{\mathrm{t}}$.

$$\mathrm{M} = \begin{pmatrix} \hat{\mathrm{n}} \cdot \hat{\mathrm{r}} & \hat{\mathrm{n}} \cdot \hat{\theta} & 0 \\ \hat{\mathrm{t}} \cdot \hat{\mathrm{r}} & \hat{\mathrm{t}} \cdot \hat{\theta} & 0 \\ 0 & 0 & 1 \end{pmatrix}. \tag{7}$$

Instead of using the displacement $\mathbf{u}(\mathrm{x}, \omega)$ directly, we break it into two parts

$$\mathbf{u}(\mathrm{x}, \omega) = \nabla \Phi(\mathrm{x}, \omega) + \nabla \times \{\Psi(\mathrm{x}, \omega) \hat{\mathrm{y}}\} \tag{8}$$

using the scalar potentials $\Phi(\mathrm{x}, \omega)$ and $\Psi(\mathrm{x}, \omega)$. Then, equation (1) separates into two independent Helmholtz equations:

$$(\nabla^2 + k^2)\, \Phi(\mathrm{x}, \omega) = 0 \tag{9a}$$

$$(\nabla^2 + l^2)\, \Psi(\mathrm{x}, \omega) = 0 \tag{9b}$$

Therefore, we replace the induced displacement fields $\mathbf{u}^0(\mathrm{x}, \omega)$ and $\mathbf{u}^1(\mathrm{x}, \omega)$ by the potentials $\Phi^0(\mathrm{x}, \omega)$, $\Psi^0(\mathrm{x}, \omega)$, $\Phi^1(\mathrm{x}, \omega)$ and $\Psi^1(\mathrm{x}, \omega)$. Similar to the acoustic case (Imhof, 1995a), we expand the potential fields as:

$$\Phi^d(\mathrm{x}, \omega) = \sum_{p=1}^{P} \sum_{n=-N}^{+N} a^d_{pn} \phi^d_{pn}(\mathrm{x}, \mathrm{x}^d_p, k^d, \omega) + e^d_\Phi \tag{10a}$$

$$\Psi^d(\mathrm{x}, \omega) = \sum_{p=1}^{P} \sum_{n=-N}^{+N} b^d_{pn} \psi^d_{pn}(\mathrm{x}, \mathrm{x}^d_p, l^d, \omega) + e^d_\Psi \tag{10b}$$

where $\phi^d_{pn}(\mathrm{x}, \mathrm{x}^d_p, k^d, \omega)$ and $\psi^d_{pn}(\mathrm{x}, \mathrm{x}^d_p, l^d, \omega)$ are solutions to either Helmholtz equation (9a) or (9b), respectively. The error terms e^d_Φ and e^d_Ψ are included not only because the series are truncated after $\pm N$ terms, but also because an expansion of this form is mathematically *non-orthogonal.*

An expansion of the form (10a) or (10b) is known as a multiple multipole (MMP) expansion (Ballisti and Hafner, 1983; Hafner, 1990). Setting P to one yields the classical eigenfunction (SMP) expansion (Morse and Feshbach, 1953). In the background region Γ^0, we choose propagating waves (Morse and Feshbach, 1953) involving the Hankel solutions $H^{(1)}_{|n|}\, e^{in\theta}$ as expansion functions ϕ^0_{pn} and ψ^0_{pn}:

$$\phi^0_{pn}(\mathrm{x}, \mathrm{x}^0_p, k^0, \omega) = H^{(1)}_{|n|}\left(k^0\, |\mathrm{x} - \mathrm{x}^0_p|\right) e^{in\theta} \tag{11a}$$

$$\psi^0_{pn}(\mathrm{x}, \mathrm{x}^0_p, l^0, \omega) = H^{(1)}_{|n|}\left(l^0\, |\mathrm{x} - \mathrm{x}^0_p|\right) e^{in\theta} \tag{11b}$$

where the expression x^0_p denotes the p^{th} center of expansion for $\Phi^0(\mathrm{x}, \omega)$ and $\Psi^0(\mathrm{x}, \omega)$. The expansion centers x^0_p have to be positioned *inside the scatterer* Γ^1 to avoid the singularity of the Hankel functions (Morse and Feshbach, 1953; Imhof, 1995a).

However, there are two possible choices for the expansions of the fields $\Phi^1(\mathbf{x},\omega)$ and $\Psi^1(\mathbf{x},\omega)$ inside the finite scatterer Γ^1. First, we can place the expansion centers $\mathbf{x}_p^1$ *inside the scatterer* ($\mathbf{x}_p^1 \in \Gamma^1$) and use expansions involving the Bessel solutions $J_{|n|}\, e^{in\theta}$ which correspond to standing waves (Morse and Feshbach, 1953).

$$\phi_{pn}^1(\mathbf{x},\mathbf{x}_p^1,k^1,\omega) = J_{|n|}\left(k^1\,|\mathbf{x}-\mathbf{x}_p^1|\right) e^{in\theta} \qquad \text{if } \mathbf{x}_p^1 \in \Gamma^1 \tag{12a}$$

$$\psi_{pn}^1(\mathbf{x},\mathbf{x}_p^1,k^1,\omega) = J_{|n|}\left(l^1\,|\mathbf{x}-\mathbf{x}_p^1|\right) e^{in\theta} \qquad \text{if } \mathbf{x}_p^1 \in \Gamma^1. \tag{12b}$$

Second, we can place the expansion centers $\mathbf{x}_p^1$ *into the background* ($\mathbf{x}_p^1 \in \Gamma^0$) and use propagating waves $H_{|n|}^{(1)}\, e^{in\theta}$ involving the Hankel functions of the first kind.

$$\phi_{pn}^1(\mathbf{x},\mathbf{x}_p^1,k^1,\omega) = H_{|n|}^{(1)}\left(k^1\,|\mathbf{x}-\mathbf{x}_p^1|\right) e^{in\theta} \qquad \text{if } \mathbf{x}_p^1 \in \Gamma^0 \tag{13a}$$

$$\psi_{pn}^1(\mathbf{x},\mathbf{x}_p^1,k^1,\omega) = H_{|n|}^{(1)}\left(l^1\,|\mathbf{x}-\mathbf{x}_p^1|\right) e^{in\theta} \qquad \text{if } \mathbf{x}_p^1 \in \Gamma^0. \tag{13b}$$

These expansions represent waves propagating from the expansion center toward the scatterer (Morse and Feshbach, 1953). Inside the scatterer, we need waves propagating in all directions. Thus, expansion centers have to be placed all around the scatterer to "illuminate" the region Γ^1 from all sides. To emphasize the difference between the expansions (12) and (13), if the expansion center $\mathbf{x}_p^1$ is placed *inside* the scatterer Γ^1, we have to use the expansions (12) by superposing Bessel solutions $J_{|n|}\, e^{in\theta}$ corresponding to standing waves. Contrary to the propagatory Hankel solutions $H_{|n|}^{(1)}\, e^{in\theta}$, the Bessel solutions do not have a singularity and may therefore be evaluated at their origins. Because the singularities of the Hankel solutions represent sources, the Hankel solutions may never be used to expand wavefields in a domain in which their expansion center $\mathbf{x}_p$, and thus their singularity, is located. By definition, the only source in the problem posed is the incident field $\mathbf{u}^{inc}$. However, if the expansion center $\mathbf{x}_p^1$ is located *outside* the scatterer, then we should use the expansions (13) with the Hankel solutions $H_{|n|}^{(1)}\, e^{in\theta}$ representing wavefields emanating from expansion center $\mathbf{x}_p^1$ propagating through the scatterer. The singularities pose no problem anymore since they are not located in the domain Γ^1 and so never contribute. Figure 5 illustrates this subtlety.

We solve for the unknown coefficients a_{pn}^d and b_{pn}^d by enforcing the boundary conditions (4a) - (4d) on M discrete matching points $\mathbf{x}_m$ along the domain boundary $\partial\Gamma_{01}$. Since we have four boundary conditions, each matching point also provides four rows of the resulting linear matrix system. Altogether, we have $4J = 2 \cdot 2 \cdot P \cdot (2N+1)$ unknown coefficients a_{pn}^d, b_{pn}^d. To simplify the notation, we eliminate an index by sequentially renumbering the double-indexed expansion functions $\phi_{pn}^d(\mathbf{x},\mathbf{x}_p^d,k^d,\omega)$ and the coefficients a_{pn}^d, which results in $\phi_j^d(\mathbf{x},\mathbf{x}_j^d,k^d,\omega)$ and a_j^d, respectively. Similarly, $\psi_{pn}^d(\mathbf{x},\mathbf{x}_p^d,l^d,\omega)$ and b_{pn}^d reduce to $\psi_j^d(\mathbf{x},\mathbf{x}_j^d,l^d,\omega)$ and b_j^d, respectively. Combining all

together, we have to solve a matrix system of the form

$$\begin{pmatrix} -\Phi_n^0 & -\Psi_n^0 & \Phi_n^1 & \Psi_n^1 \\ -\Phi_t^0 & -\Psi_t^0 & \Phi_t^1 & \Psi_t^1 \\ -\Phi_{nn}^0 & -\Psi_{nn}^0 & \Phi_{nn}^1 & \Psi_{nn}^1 \\ -\Phi_{nt}^0 & -\Psi_{nt}^0 & \Phi_{nt}^1 & \Psi_{nt}^1 \end{pmatrix}_{4M\times 4J} \cdot \begin{pmatrix} \mathbf{a}^0 \\ \mathbf{b}^0 \\ \mathbf{a}^1 \\ \mathbf{b}^1 \end{pmatrix}_{4J} = \begin{pmatrix} \mathbf{u}_n \\ \mathbf{u}_t \\ \boldsymbol{\sigma}_{nn} \\ \boldsymbol{\sigma}_{nt} \end{pmatrix}_{4M} + \begin{pmatrix} \mathbf{e}_n \\ \mathbf{e}_t \\ \mathbf{e}_{nn} \\ \mathbf{e}_{nt} \end{pmatrix}_{4M} \tag{14}$$

where the submatrices Φ_n^d and Ψ_n^d denote the normal displacements u_n at the matching points due to ϕ_j^d and ψ_j^d, respectively. The submatrices Φ_t^d and Ψ_t^d are the same except for the tangential component u_t of the displacement. The submatrices Φ_{nn}^d and Ψ_{nn}^d contain the normal stresses σ_{nn}, while Φ_{nt}^d and Ψ_{nt}^d contain the tangential stresses σ_{nt}.

Defining the matching points by their location $\mathbf{x}_m$, we evaluate these submatrices as

$$\left[\Phi_{n,mj}^d\right] = u_n\left(\phi_j^d(\mathbf{x}_m)\right) \qquad \left[\Psi_{n,mj}^d\right] = u_n\left(\psi_j^d(\mathbf{x}_m)\right) \tag{15a}$$

$$\left[\Phi_{t,mj}^d\right] = u_t\left(\phi_j^d(\mathbf{x}_m)\right) \qquad \left[\Psi_{t,mj}^d\right] = u_t\left(\psi_j^d(\mathbf{x}_m)\right) \tag{15b}$$

$$\left[\Phi_{nn,mj}^d\right] = \sigma_{nn}\left(\phi_j^d(\mathbf{x}_m)\right) \qquad \left[\Psi_{nn,mj}^d\right] = \sigma_{nn}\left(\psi_j^d(\mathbf{x}_m)\right) \tag{15c}$$

$$\left[\Phi_{nt,mj}^d\right] = \sigma_{nt}\left(\phi_j^d(\mathbf{x}_m)\right) \qquad \left[\Psi_{nt,mj}^d\right] = \sigma_{nt}\left(\psi_j^d(\mathbf{x}_m)\right) \tag{15d}$$

where we used the index $m \in \{1,\ldots,M\}$ to denote the matching points $\mathbf{x}_m$, the index $j \in \{1,\ldots,J\}$ for the expansion functions ϕ_j^d, ψ_j^d and the index $d \in \{0,1\}$ for the domain. The expression $u_n\left(\phi_j^d(\mathbf{x}_m)\right)$ represents the normal displacement due to the expansion function ϕ_j^d evaluated at the matching point $\mathbf{x}_m$. The others are to be interpreted similarly.

The vectors $\mathbf{a}^0$, $\mathbf{b}^0$, $\mathbf{a}^1$, and $\mathbf{b}^1$ in equation (14) contain the unknown coefficients a_j^0, b_j^1, a_j^1, b_j^1 for the expansion functions ϕ_j^0, ψ_j^0, ϕ_j^1, and ψ_j^1, respectively. The vectors $\mathbf{u}_n$, $\mathbf{u}_t$, $\boldsymbol{\sigma}_{nn}$, and $\boldsymbol{\sigma}_{nt}$ hold the normal and tangential displacements as well as normal and tangential stresses at the M matching points due to the incident field $\mathbf{u}^{inc}$.

$$\left[u_{n,m}\right] = u_n^{inc}(\mathbf{x}_m) \qquad \left[u_{t,m}\right] = u_t^{inc}(\mathbf{x}_m) \tag{16a}$$

$$\left[\sigma_{nn,m}\right] = \sigma_{nn}^{inc}(\mathbf{x}_m) \qquad \left[\sigma_{nt,m}\right] = \sigma_{nt}^{inc}(\mathbf{x}_m) \tag{16b}$$

Finally, the matrix equation (14) contains the residual vectors $\mathbf{e}_n$, $\mathbf{e}_t$, $\mathbf{e}_{nn}$, $\mathbf{e}_{nt}$ with the misfit of the boundary conditions at the individual matching points.

The extension to multiple scattering objects is straightforward and follows exactly the acoustic case (Imhof, 1995a). Assuming that the scatterers do not intersect, an MMP expansion has to be set up from each scatterer $d \in \{1,\ldots,D\}$. Thus for the fields in the background domain Γ^0, we obtain

$$\Phi^0(\mathbf{x},\omega) = \sum_{d}\sum_{p}\sum_{n} a_{pn}^d \phi_{pn}^d(\mathbf{x}, \boldsymbol{x}_p^d, k^0, \omega) + e_\Phi^0 \tag{17a}$$

$$\Psi^0(\mathbf{x},\omega) = \sum_{d}\sum_{p}\sum_{n} b_{pn}^d \psi_{pn}^d(\mathbf{x}, \boldsymbol{x}_p^d, l^0, \omega) + e_\Psi^0 \tag{17b}$$

where x_p^d denotes the centers for the expansions of $\Phi^0(\mathbf{x},\omega)$ and $\Psi^0(\mathbf{x},\omega)$. The expansion centers x_p^d have to be positioned *inside the scatterer* Γ^d to avoid the effect of the singularity of the Hankel functions. The fields inside the scatterers Γ^d can still be expressed by (10).

NUMERICAL RESULTS

To obtain a seismogram in the domain $d \in \{0,1\}$, we must evaluate the Fourier integral

$$\mathbf{u}^d(\mathbf{x},t) = \int_{-\infty}^{+\infty} \mathbf{U}^d(\mathbf{x},\omega) e^{i\omega t}\, d\omega \tag{18}$$

where

$$\mathbf{U}^d(\mathbf{x},\omega) = \delta_{0d}\, \mathbf{u}^{inc}(\mathbf{x},\omega) + \sum^{p}\sum^{n} a_{pn}^d \cdot \nabla \phi_{pn}^d(\mathbf{x},\mathbf{x}_p^d,k^d,\omega) + b_{pn}^d \cdot \nabla \times \left\{ \psi_{pn}^d(\mathbf{x},\mathbf{x}_p^d,l^d,\omega)\hat{\mathbf{y}}. \right\} \tag{19}$$

To perform the operation, one needs to move the singularities of $\mathbf{U}^d(\mathbf{x},\omega)$ off the real ω axis. This may be done by adding a small imaginary component ω_I to the frequency (Bouchon and Aki, 1977).

$$\omega = \omega_R + i\omega_I \qquad \text{where} \quad \omega_I > 0. \tag{20}$$

The singularities in $\mathbf{U}^d(\mathbf{x},\omega)$ correspond to resonances, surface modes and creeping waves induced by the scatterers. The use of the complex frequency has the effect of smoothing the spectrum and enhancing the first motions relative to later arrivals. This attenuating effect of the imaginary frequency component can be removed from the final time domain solution by a multiplication with $e^{\omega_I t}$.

$$\mathbf{u}^d(\mathbf{x},t) = e^{\omega_I t} \int_{-\infty}^{+\infty} \mathbf{U}^d(\mathbf{x},\omega) e^{i\omega_R t}\, d\omega_R. \tag{21}$$

Due to the complex frequency, the Bessel and Hankel functions have to be evaluated with a complex argument (Abramowitz and Stegun, 1964; Amos, 1986). In practice, the integral is approximated by a discrete Fourier transformation (DFT). Its use will result in aliasing in the time-domain due to the periodicity in time and frequency as implied by the DFT (Brigham, 1988). Again, this effect can be reduced by the small imaginary part ω_I which attenuates disturbances not belonging to the time window of interest.

The matrix system is solved by QR decomposition using Givens rotations (Wilkinson, 1988) which allows one to build the matrix system row by row while storing only a triangular matrix with dimensions of the number of unknowns in the computer memory (George and Heath, 1980). Since we want to calculate synthetic seismograms using the frequency domain method, we have to solve the scattering problem for a range of

frequencies and later apply a Fourier transformation to obtain the seismograms. All these problems can be solved independently of each other. Consequently, the algorithm is implemented on an nCUBE2 parallel computer where each processor will calculate a few frequencies.

We now show how the method performs solving a simple problem using different ways to discretize it. For the sake of simplicity, the incident field $\mathbf{u}^{inc}$ is an explosive line source modulated with a Ricker pulse (Hosken, 1988) of 50 Hz center frequency. Altogether, 64 receivers will measure the u_z component of the total field $\mathbf{u}^0(\mathbf{x}, t)$ in the background.

The rather generic scatterer is shown in Figure 6. Its size is roughly 240 m in length and 50 m in thickness. The density and velocities in the background are $\rho^0 = 2000\,\mathrm{kg/m^3}$, $\alpha^0 = 2000\,\mathrm{m/s}$ and $\beta^0 = 1155\,\mathrm{m/s}$, respectively. In the scatterer, the density and velocities are $\rho^1 = 2500\,\mathrm{kg/m^3}$, $\alpha^1 = 3000\,\mathrm{m/s}$ and $\beta^1 = 1732\,\mathrm{m/s}$. Thus, the Poisson's ratio is the same for both regions ($\sigma = 0.25$). The center frequency of 50Hz yields an incident wavelength of 40 m which roughly equals the thickness of the scatterer.

In order to have a reference seismogram in which to compare the different MMP solutions, we calculate the solution using a finite difference (FD) method (Kelly *et al.*, 1976; Peng and Toksöz, 1994). The resulting reference seismogram is shown in Figure 7. As a measure of how well the MMP seismogram $u_z^{MMP}(r,t)$ correlates with the FD reference seismogram $u_z^{FD}(r,t)$, we define the root mean square error (RMSE) and the relative root mean square error (RRMSE). The RMSE is defined by the squared difference between the two seismograms

$$\mathrm{RMSE} = \frac{1}{\sqrt{RT}}\sqrt{\sum_{r=1}^{R}\sum_{t=1}^{T}\left\{u_z^{MMP}(r,t) - u_z^{FD}(r,t)\right\}^2} \tag{22a}$$

where $u_z(r,t)$ denotes the vertical displacement measured at recorder r at time sample t. $R = 64$ is the number of recorders and $T = 256$ is the total number of time samples. The RRMSE is defined by the squared relative difference between the two seismograms

$$\mathrm{RRMSE} = \frac{1}{\sqrt{N'}}\sqrt{\sum^{r'}\sum^{t'}\left\{\frac{u_z^{MMP}(r',t') - u_z^{FD}(r',t')}{u_z^{MMP}(r',t') + u_z^{FD}(r',t')}\right\}^2} \tag{22b}$$

where we drop terms for which $\frac{1}{2}\left|u_z^{MMP}(r',t')\right| + \frac{1}{2}\left|u_z^{FD}(r',t')\right|$ is below 50 dB relative to its maximum value. N' is simply the number of terms above the threshold. The use of the threshold prevents the RRMSE from being dominated by minute amplitudes while still accounting for smaller, yet visible features in the seismograms.

MMP Versus the Finite Difference Reference Solution

As a first example, we present both a solution obtained by MMP expansions and the reference solution as obtained by finite differences. For the finite difference case, we used

a grid spacing of 1 m and a grid of 750 by 750 points. The grid dimensions are larger than needed to prevent reflections from imperfectly absorbing boundaries to reach the receivers. The timestep used is 0.05 ms. The runtime on an nCUBE2 using 64 nodes was 23 minutes. The seismogram calculated by finite differences is shown in Figure 7.

For the MMP expansion, we used a total of 256 expansion functions, 128 matching points, 8 expansion centers and 64 frequencies. The resulting runtime on an nCUBE2, again using 64 nodes, was 12 minutes. Figure 8 shows the seismogram calculated using the MMP expansion. The two methods yield the same result. As can be seen, they agree very well in both traveltimes and phases. To facilitate the comparison, we placed 5 receivers inside the scatterer and positioned 9 additional receivers around the scatterer. The exact geometry is presented in Table (1) and depicted in Figure 9. The normalized traces for both the FD and MMP solutions are overlaid in Figure 10. For all receiver positions, the two solutions match perfectly even for small amplitudes.

Effect of the Number of Expansion Functions

As a second experiment, we study how the number of expansion functions affects the solutions obtained. We start with a total of 32 expansion functions located at 8 expansion centers. Thus, we have one monopole for each potential and each region at every expansion center. We calculate the resulting seismogram and estimate the resulting RMSE and RRMSE. Then, we double the number of expansion functions per expansion center, calculate the seismograms anew, estimate the RMSE, estimate the RRMSE, and so on, until a total of 4048 expansion functions are used. The number of matching points is kept constant at $M = 2048$ while the number of expansion centers is kept constant at $P = 8$. Figure 11 shows the resulting RMSE and RRMSE as functions of the total number of expansion functions used. A first observation is that 256 expansion functions seem to be the critical amount. Using fewer expansion functions yields solutions that cannot capture important features of the true seismogram; hence, the solutions do not converge. Figure 12 shows a seismogram which is typical for an unconverged solution. The seismogram was obtained with only 64 expansion functions. For more than 256 expansion functions, we have convergence where both RMSE and RRMSE decrease slowly with an increasing number of expansions functions. As a reminder, the well-converged MMP solution presented in Figures 8 and 10 was also calculated with 256 expansion functions and 8 expansion centers.

MMP versus SMP Expansion

The next numerical experiment performed shows the enhanced convergence of the MMP expansion compared to the classical eigenfunction expansion (SMP). As mentioned previously, the SMP expansion corresponds to using only one expansion center in (10a) or (10b). We perform the same experiment as before but use only one expansion center. Again, we start with one expansion function per domain and scalar potentials Φ and Ψ, which yield 4 expansion functions altogether. We calculate the resulting seis-

mograms and estimate the RMSE and RRMSE. The resulting seismogram is shown in Figure 13. The seismogram is clean enough to be mistaken as correct but has no resemblance with the correct solution shown in Figure 7. Then we double the number of expansion functions per expansion center, calculate the seismograms, estimate the RMSE, the RRMSE, and so on. The number of matching points is again kept constant at $M = 2048$. Figure 11 shows the resulting RMSE and RRMSE as functions of the total number of expansion functions used. We notice that the MMP expansion using 8 expansion centers always performs better than the classical SMP. In addition, using more than 256 expansion functions in the SMP expansion yields no useful results. The solutions obtained begin to diverge rapidly. This is an effect due to the expansion functions of higher-order violating the sampling condition (Hafner, 1990; Imhof, 1995a). The maximum order N^{max} of a multipole is given by the largest angle φ^{max} between any two adjacent matching points and the location of the multipole:

$$N^{max} < \frac{\pi}{\varphi^{max}}. \tag{23}$$

The increased error in the SMP expansion between 16 and 64 expansion functions is an effect of the error measures (22) which are strongly affected by phase shifts. Contrary to the MMP expansion, an SMP expansion cannot solve the problem posed in Figure 7.

Effect of Number and Location of Expansion Centers

The next numerical experiment is to examine the importance and effect of the number, location and distribution of the expansion centers. As mentioned above, we have the choice of placing the expansion centers for the $\Phi^1(\mathbf{x}, \omega)$ and $\Psi^1(\mathbf{x}, \omega)$ fields either in or outside the scatterer, and thus expanding either into standing waves $J_{|n|}(kr)\, e^{in\theta}$ or into propagating waves $H^{(1)}_{|n|}(kr)\, e^{in\theta}$. We will use both to study the difference.

We calculate the solutions for a range of expansion centers while keeping the total number of expansion functions constant at 256. Also, the number of matching points is kept constant at 256. Thus, the overall computational effort to calculate one seismogram is kept constant. The resulting RMSE and RRMSE are shown in Figure 14. It is surprising how broad the 'U'-shaped, minimal-error region is. The whole range from 5 to 15 expansion centers seems to converge. Indeed, the minimal RMSE and RRMSE obtained by 11 expansion centers are only slightly better than any other discretization employing 5 to 15 centers. Remarkably, MMP expansions are very insensitive to the actual discretization used! Neither the number of expansion centers nor the kind of expansions changes the RMSE or RRMSE by much, although the use of $H^{(1)}_{|n|}(kr)\, e^{in\theta}$ produces smoother RMSE and RRMSE curves.

The pathological case with 23 expansion centers shows that the errors increase dramatically when too many expansion centers are used. In this particular case, the expansion centers are separated by only a quarter of the dominant wavelength. The different expansion functions begin to interact by approximating higher order solutions to the wave equation. It is well-known that two monopoles of opposite sign placed closely

together are equivalent to a dipole (Morse and Feshbach, 1953). Thus, the matrix system becomes badly conditioned since each expansion center could be replaced by the adjacent ones. Moreover, we add more similar equations to the matrix system which renders it more ill-conditioned.

For comparison, we also use a simple boundary element (BEM) discretization with the same number of matching points and expansion functions. Along the boundary in between matching points, we place rotational and compressional monopole sources. As in the MMP cases, we use point matching and solve the system in the least-squares sense. The resulting large RMSE and RRMSE indicate that the seismogram obtained is not correct. Indeed, it contains mainly the reflections from the top of the scatterer. Reflections from the bottom as well as internal multiple scattered phases are mostly missing.

Effect of the Number of Matching Points

The final numerical experiment examines how the number of matching points affects the solutions. Actually, the ratio between the total number of equations in the matrix system and the number of expansion functions used—not the number of matching points—is the important parameter. In accordance with the earlier experiments, we choose 11 expansion centers and keep the number of expansion functions constant at 256. Since each matching point provides 4 equations (one for each boundary condition), we start out with 64 matching points along the boundary which provide 256 equations altogether. We calculate the resulting seismogram, estimate the RMSE and RRMSE, double the number of matching points, and so on. Figure 15 shows the resulting errors against the number of equations per expansion function. Since the expansion is non-orthogonal, it is not surprising that we get large errors when we use as many equations as we have unknowns. Using twice as many equations as unknowns provides the optimal result. Afterwards, the more equations we add, the more the RMSE and RRMSE increase because the matrix system becomes more ill-conditioned with each additional equation we add. The result is more errors due to roundoff and other numerical effects.

Using twice as many equations as unknowns yields a distance of 4 m between matching points. This spacing corresponds to 10 matching points per dominant wavelength of 40 m. Assuming that the highest frequency in the propagating seismic Ricker pulse is 3 times the center frequency of 50 Hz (Hosken, 1988), the boundary is sampled with 3 matching points per wavelength for the highest frequency. The sampling theorem which states that the boundary has to be sampled at least twice per wavelength to prevent aliasing (Bouchon and Aki, 1977), is just satisfied. Thus, it is also theoretically justified to use about 10 matching points per dominant wavelength.

DISCUSSION AND CONCLUSIONS

Combining these numerical experiments with prior experiences with electromagnetic (Hafner, 1990) and acoustical MMP methods (Imhof, 1995a), we obtain a set of empirical

rules on how to discretize elastic scattering problems. A very important parameter is the radius of greatest influence of a multipole which is $\sqrt{2}$ times the distance between the center of expansion and the closest matching point.

- The radius of greatest influence should be on the order of the dominant wavelength.
- No expansion center should be within the radius of greatest influence of any other expansion center.
- There should be ≈ 10 matching points per dominant wavelength
- There has to be at least half a matching point per expansion function or similarly two equations per expansion function.
- The maximum order N of a multipole is given by the sampling theorem: $N < \pi/\varphi^{max}$ where φ^{max} is the maximal angle φ under which two adjacent matching points located within the radius of greatest influence are seen by the respective multipole.
- Expansions of the form $H^{(1)}_{|n|}\,(kr)\;e^{in\theta}$ should not be used for the region where their expansion center $\mathbf{x}_p$ is located. Expansions of the form $J_{|n|}\,(kr)\;e^{in\theta}$ should only be used for bounded domains. The expansion center $\mathbf{x}_p$ has to be located inside this region.

The above rules, except the last one, are general guidelines, but adhering to them generally yields satisfactory results. As the numerical experiments show, all parameters can be varied by large amounts while only perturbing the resulting solution. The MMP method is not very sensitive to the actual discretization used.

We showed that the MMP expansion converges faster than the classical multipole or simple boundary element expansions for complex scattering geometries. The method can solve scattering problems involving harmonic sources by using Fourier synthesis to calculate seismograms. For a homogeneous scatterer embedded in a homogeneous background, we found the MMP expansions yield the same degree of accuracy as the finite difference method. For the MMP method, the computational effort is related to the interface area of the embedded scatterers and thus to the number of expansion functions and matching points needed. For the FD method, the computational effort relates to the volume containing the sources, receivers and scatterers. For problems where the distances between sources, receivers and scatterers are large, MMP expansions are competitive. Also, due to its spectral nature, attenuation can easily be accounted for. For problems where heterogeneous scatterers are embedded in a homogeneous background, hybridized schemes with finite elements can be devised (Imhof, 1995b).

In conclusion, the MMP method is well-suited for a large range of scattering problems since both acoustic and elastic media with different boundary conditions (fluid-fluid, fluid-elastic, elastic-elastic and others) can be treated exactly the same way in this algorithm.

ACKNOWLEDGMENTS

This work was supported by the Air Force Office of Scientific Research under contract no. F49620-93-1-0424DEF and by the Reservoir Delineation Consortium at the Massachusetts Institute of Technology. . The author was supported the nCUBE Fellowship. The author thanks Dr. C. Hafner and Dr. L. Bomholt, both at the Eidgenösische Technische Hochschule in Zürich, Switzerland, for their helpful comments and discussions.

REFERENCES

Abramowitz, M. and Stegun, I. A., editors (1964). *Handbook of mathematical functions*. Dover, New York.

Amos, D. E. (1986). ALGORITHM 644: a portable package for Bessel functions of a complex argument and nonnegative order. *ACM Transactions on Mathematical Software*, **12**(3), 265–273.

Ballisti, R. and Hafner, C. (1983). The multiple multipole method in electro- and magnetostatic problems. *IEEE Transactions on Magnetics*, **19**(6), 2367–2370.

Boström, A. (1980). Scattering by a smooth elastic obstacle. *Journal of the Acoustical Society of America*, **67**(6), 1904–1912.

Bouchon, M. and Aki, K. (1977). Discrete wavenumber representation of seismic-source wave fields. *Bulletin of the Seismological Society of America*, **67**(2), 259–277.

Bowman, J. J., Senior, T. B. A., and Uselenghi, P. L. E., editors (1969). *Electromagnetic and acoustic scattering by simple shapes*. North-Holland Publishing Company, Amsterdam.

Brebbia, C. A. and Dominguez, J., editors (1989). *Boundary Elements, an introductory course*. McGraw-Hill, New York.

Brigham, E. O. (1988). *The fast Fourier transform and its applications*. Prentice Hall, Englewood Cliffs, NJ, 2nd edition.

Chin, R. C., Hedstrom, G. W., and Thigoen, L. (1984). Matrix methods in synthetic seismograms. *Geophysical Journal of the Royal Astronomical Society*, **77**, 483–502.

George, A. and Heath, M. T. (1980). Solutions of sparse linear least squares problems using Givens rotations. *Linear algebra and its applications*, **34**, 69–83.

Haartsen, M. W., Bouchon, M., and Toksöz, M. N. (1994). A study of seismic acoustic wave propagation through a laterally varying medium using the boundary-integral-equation- discrete wave-number method. *Journal of the Acoustical Society of America*, **96**, 3010–3021.

Hafner, C. (1990). *The generalized multipole technique for computational electromagnetics*. Artech House, Inc, Boston.

Hafner, C. (1993). On the design of numerical methods. *IEEE Antennas and Propagation Magazine*, **35**(4), 13–21.

Hosken, J. W. (1988). Ricker wavelets in their various guises. *First Break*, **6**(1), 24–33.

Imhof, M. G. (1995a). Multiple multipole expansions for acoustic scattering. *Journal of the Acoustical Society of America*, **97**(2), 754–763.

Imhof, M. G. (1995b). Scattering of acoustic and elastic waves using a hybrid multiple multipole expansions – finite element technique. *Journal of the Acoustical Society of America*. submitted.

Kelly, K. R., Ward, R. W., Treitel, S., and Alford, R. M. (1976). Synthetic seismograms: a finite difference approach. *Geophysics*, **41**(1), 2–27.

Kennett, B. L. (1983). *Seismic wave propagation in stratified media*. Cambridge University Press.

Lakhtakia, A., Varadan, V. K., and Varadan, V. V. (1984). Iterative extended boundary condition method for scattering by objects of high aspect ratio. *Journal of the Acoustical Society of America*, **76**(3), 906–912.

Morse, P. M. and Feshbach, H. (1953). *Methods of Theoretical Physics*. McGraw-Hill.

Müller, G. (1985). The reflectivity method: a tutorial. *Journal of Geophysics*, **58**, 153–174.

Pao, Y. H. and Mow, C. C. (1973). *Diffraction of Elastic Waves and Dynamic Stress Concentrations*. The Rand Corporation, New York.

Papworth, T. J. (1985). Seismic exploration over basalt covered areas in the U.K. *First Break*, **3**(4), 20–32.

Peng, C. and Toksöz, M. N. (1994). An optimal absorbing boundary condition for finite difference modeling of acoustic and elastic wave propagation. *Journal of the Acoustical Society of America*, **95**(2), 733–745.

Pritchett, W. C. (1990). Problems and answers in recording reflections from beneath karst or volcanic surfaces. In *60th Annual Internat. Mtg., Soc. Expl. Geophys., Expanded Abstracts*, volume 90, pages 922–925.

Pujol, J., Fuller, B. N., and Smithson, S. B. (1989). Interpretation of a vertical seismic profile conducted in the Columbia Plateau basalts. *Geophysics*, **54**(10), 1258–1266.

Waterman, P. C. (1976). Matrix theory of elastic wave scattering. *Journal of the Acoustical Society of America*, **60**(3), 567–580.

Wilkinson, J. H. (1988). *The Algebraic Eigenvalue Problem*. Oxford University Press.

Wu, R. S. and Aki, K. (1985). Elastic wave scattering by a random medium and small-scale inhomogeneities in the lithosphere. *Journal of Geophysical Research*, **90**, 10261–10273.

Receiver	x	z	Comments
1	-70.0	0.0	incident field does not contribute
2	70.0	0.0	incident field does not contribute
3	70.0	-200.0	
4	0.0	-200.0	
5	-70.0	-200.0	
6	-110.0	-110.0	inside scatterer
7	-50.0	-100.0	inside scatterer
8	0.0	-100.0	inside scatterer
9	50.0	-100.0	inside scatterer
10	105.0	-110.0	inside scatterer
11	-150.0	-200.0	
12	150.0	-200.0	
13	-150.0	200.0	
14	150.0	200.0	

Table 1: Locations of the receivers used in the comparison of the MMP solution to the FD solution. The source location is the origin of the coordinate system used.

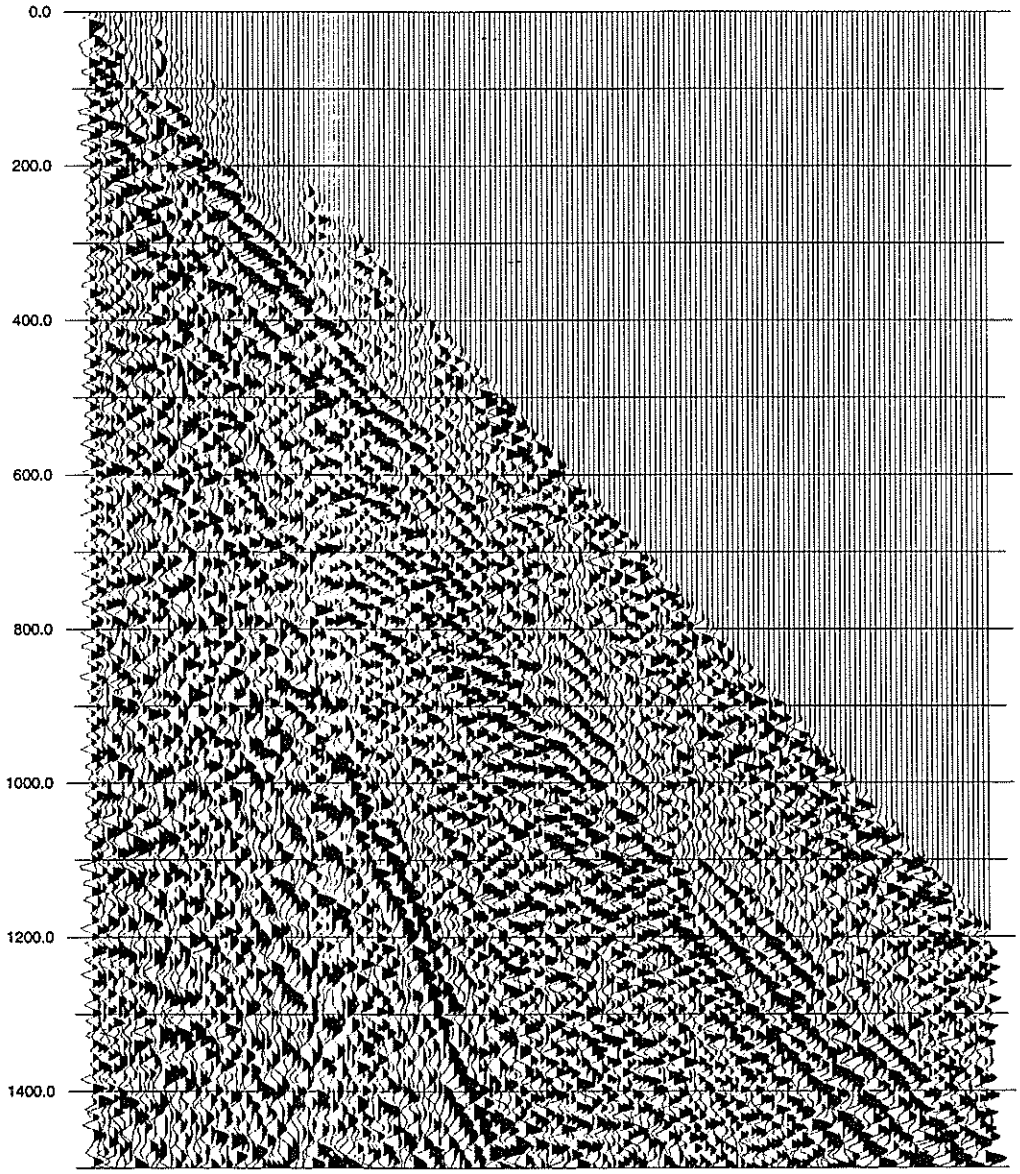

Figure 1: The first 1.5 s of a seismogram shot with the source located in a valley.

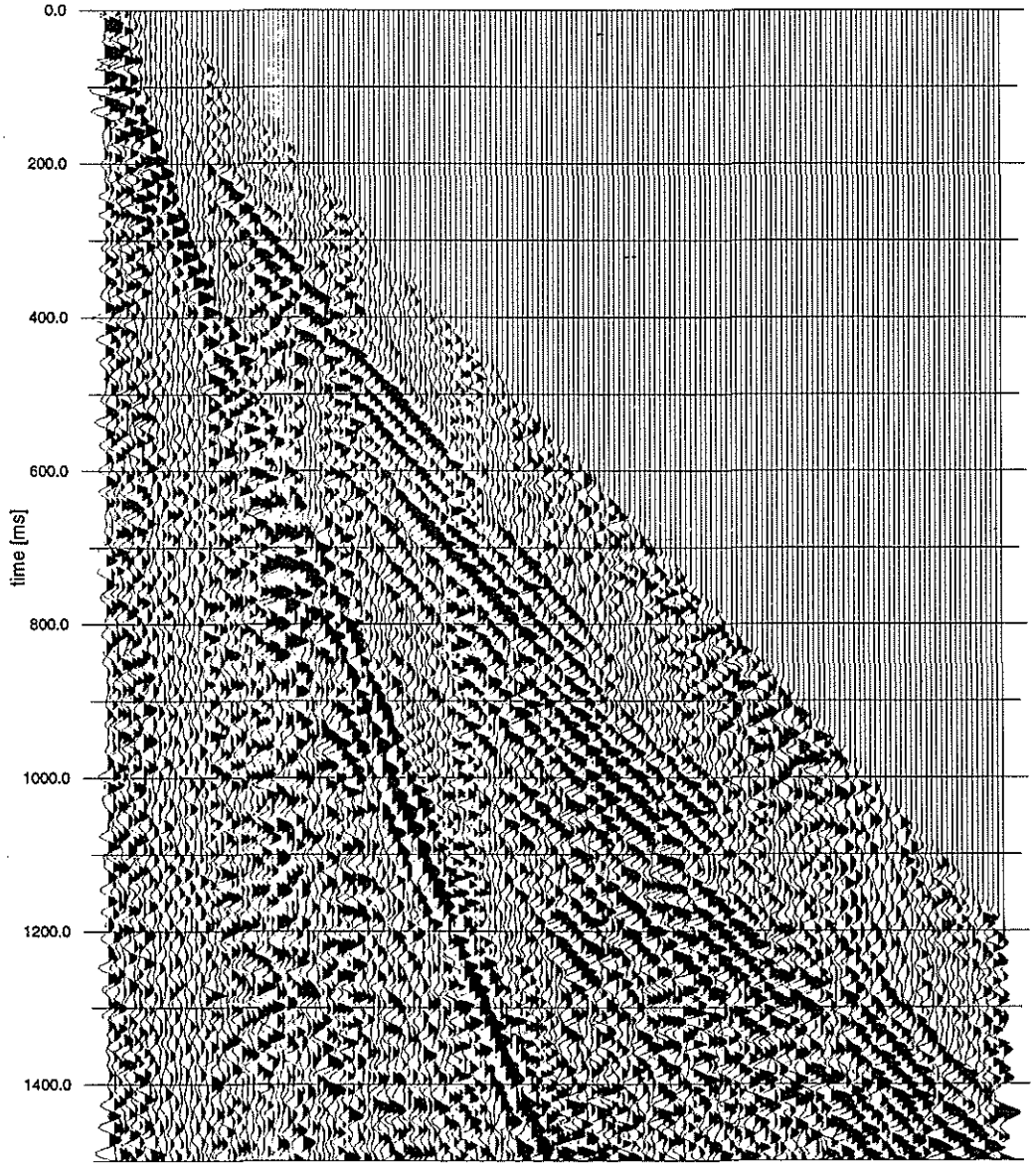

Figure 2: The first 1.5 s of a seismogram shot with the source on top of a mesa at station 1153.

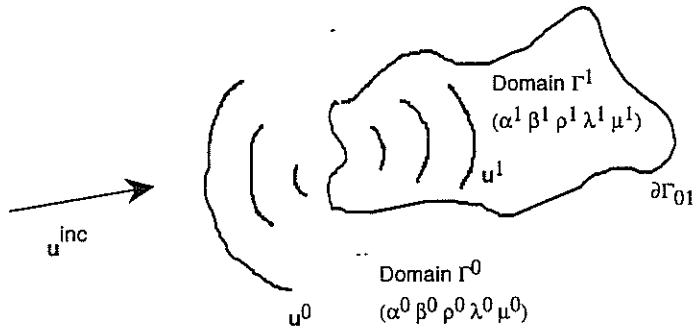

Figure 3: Schematic representation of the scattering experiment. An incident field $\mathbf{u}^{inc}(\mathbf{x},\omega)$ illuminates a bounded two-dimensional inhomogeneity which induces a scattered field $\mathbf{u}^0(\mathbf{x},\omega)$ in the background medium $(\alpha^0,\beta^0,\rho^0)$ as well as a field $\mathbf{u}^1(\mathbf{x},\omega)$ in the scatterer itself $(\alpha^1,\beta^1,\rho^1)$.

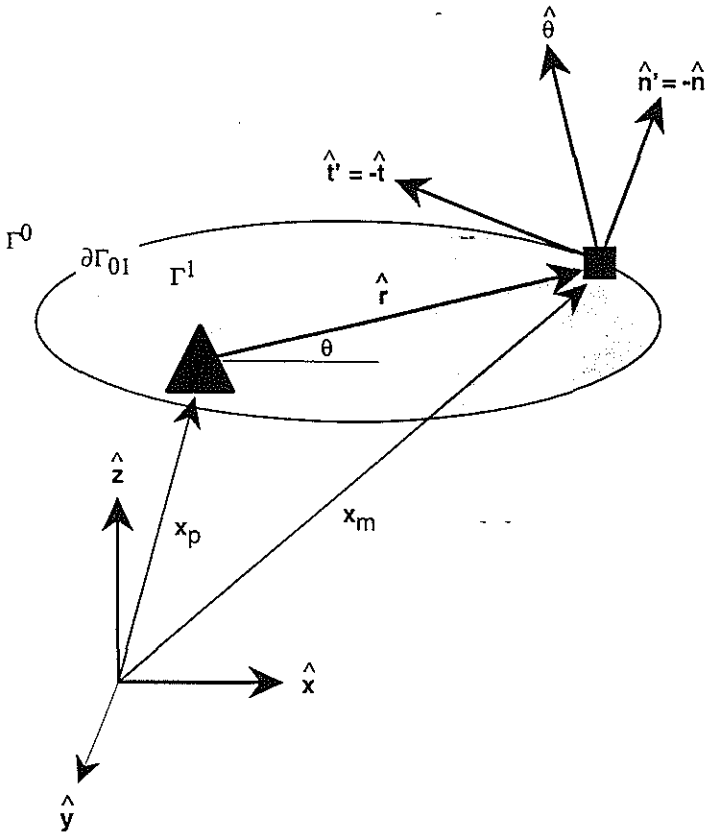

Figure 4: Schematic of the coordinate systems used. In addition to the global cartesian coordinate frame (x, z, y), local cylindrical systems (r, θ, y) and local cartesian systems (n, t, y) are used. The cylindrical coordinate systems (r, θ, y) have their origins at the expansion centers $\mathbf{x}_p$ (triangles) and are used to express the expansion functions ϕ^d_{pn} and ψ^d_{pn}. The boundary Γ_{01} between the scatterer and background is defined by discrete matching points (squares) located at $\mathbf{x}_m$, where the normal $\hat{\mathbf{n}}$ and the tangential $\hat{\mathbf{t}}$ directions are specified. The normal direction $\hat{\mathbf{n}}$ is defined to point from the background Γ^0 into the scatterer Γ^1. The boundary conditions are expressed in the local systems (n, t, y).

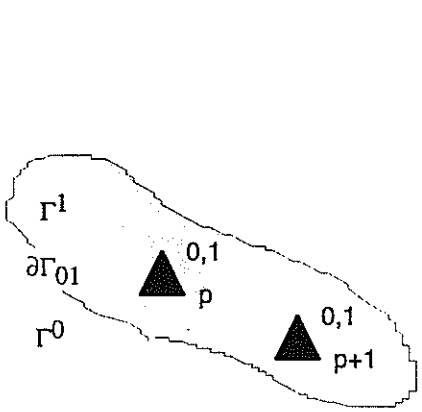

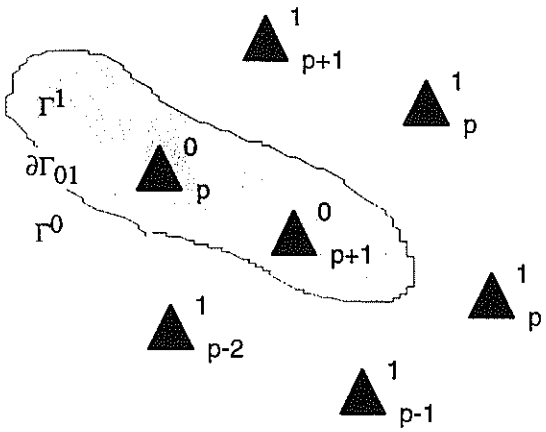

$$\Phi^0 = \sum\sum a^0_{pn} H^{(0)}_{|n|}(k^0 r^0_p) e^{in\theta}$$
$$\Psi^0 = \sum\sum b^0_{pn} H^{(0)}_{|n|}(l^0 r^0_p) e^{in\theta}$$
$$\Phi^1 = \sum\sum a^1_{pn} J_{|n|}(k^1 r^1_p) e^{in\theta}$$
$$\Psi^1 = \sum\sum b^1_{pn} J_{|n|}(l^1 r^1_p) e^{in\theta}$$

$$\Phi^0 = \sum\sum a^0_{pn} H^{(0)}_{|n|}(k^0 r^0_p) e^{in\theta}$$
$$\Psi^0 = \sum\sum b^0_{pn} H^{(0)}_{|n|}(l^0 r^0_p) e^{in\theta}$$
$$\Phi^1 = \sum\sum a^1_{pn} H^{(0)}_{|n|}(k^1 r^1_p) e^{in\theta}$$
$$\Psi^1 = \sum\sum b^1_{pn} H^{(0)}_{|n|}(l^1 r^1_p) e^{in\theta}$$

Figure 5: Basis functions can either contain Hankel solutions $H_n\, e^{in\theta}$ or Bessel solutions $J_n\, e^{in\theta}$. If the same expansion center $\mathbf{x}^0_p = \mathbf{x}^1_p$ is to be used for both ϕ^0_p and ϕ^1_p, the inside field Φ^0 has to be expanded using the Bessel solutions $J_n\, e^{in\theta}$ representing standing waves. If the inside and the outside scattered field are represented by Hankel solutions $H_n\, e^{in\theta}$, different expansion centers $\mathbf{x}^0_p$ and $\mathbf{x}^1_p$ have to be used. Expansion centers are depicted by a triangle.

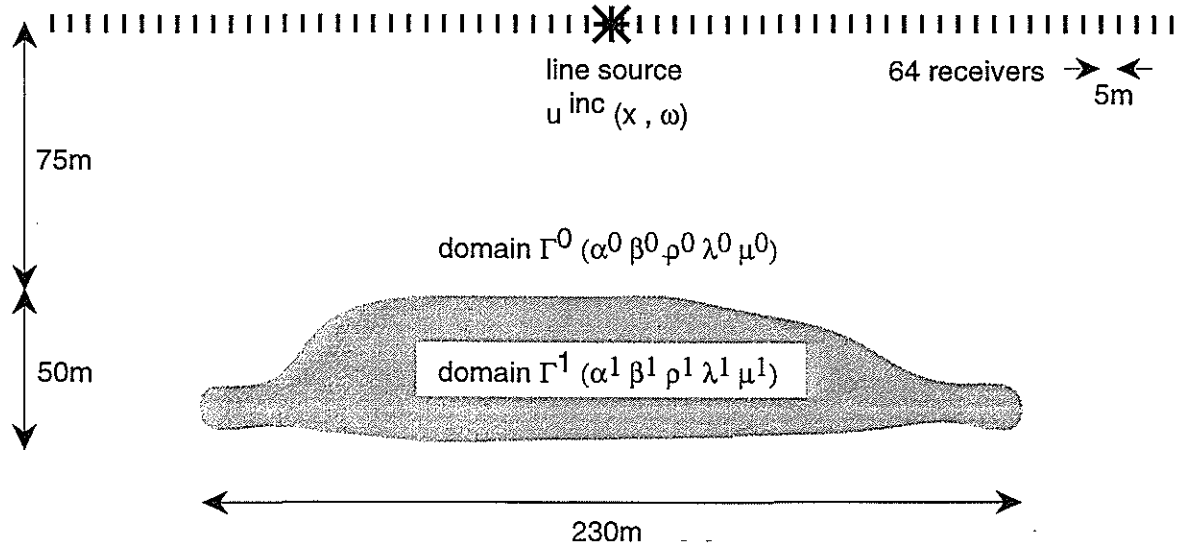

Figure 6: Generic scatterer used for numerical experiments. The scatterer is illuminated by an explosive line source modulated by a Ricker pulse of 50Hz center frequency. The density and the velocities in the background domain Γ^0 are $\rho = 2000\,\mathrm{kg/m^3}$, $\alpha^0 = 2000\,\mathrm{m/s}$ and $\beta^0 = 1155\,\mathrm{m/s}$. Density and velocities in the scatterer Γ^1 are $\rho = 2500\,\mathrm{kg/m^3}$, $\alpha^1 = 3000\,\mathrm{m/s}$ and $\beta^1 = 1732\,\mathrm{m/s}$. The Poisson's ratio is the same for both regions ($\sigma = 0.25$).

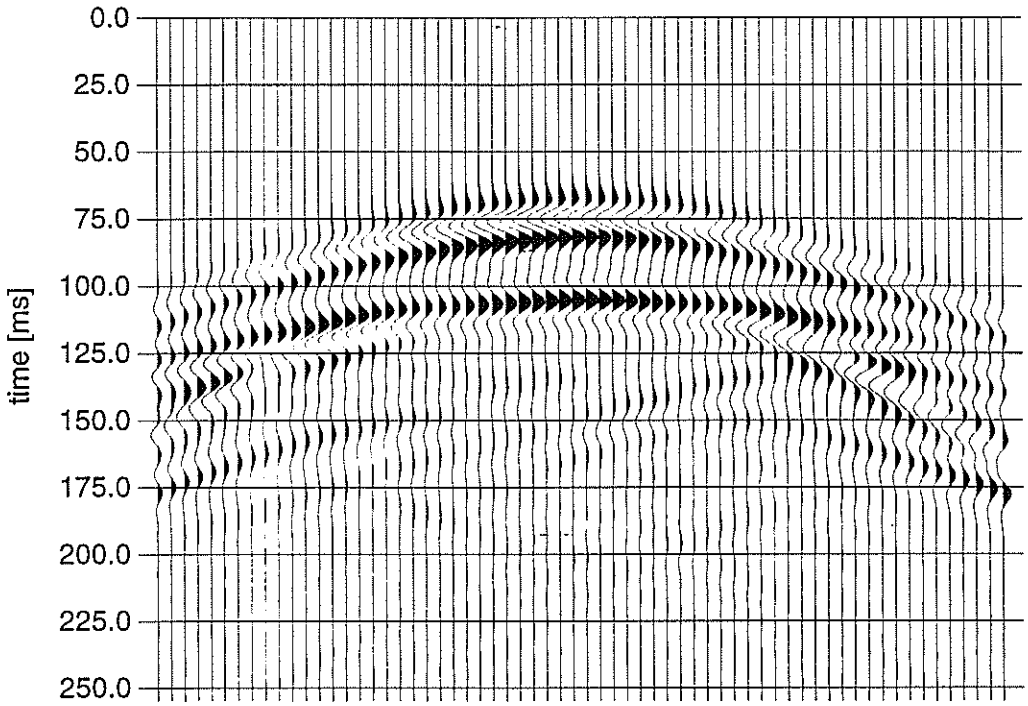

Figure 7: The seismogram of the model shown in Figure 6 calculated using a finite difference method. This seismogram is used as a reference to compare those calculated with different MMP discretizations.

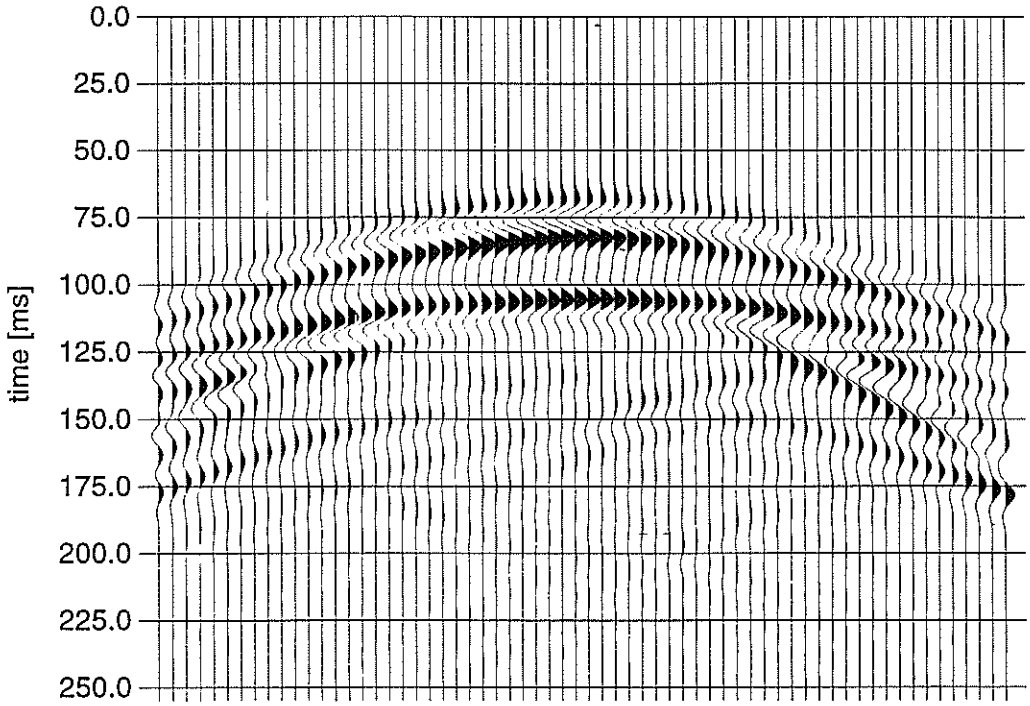

Figure 8: The seismogram of the model shown in Figure 6 calculated using the MMP algorithm. Altogether, 256 expansion functions, 8 expansion centers, 128 matching points and 64 frequencies were used. As can be seen, the MMP solution agrees very well with the finite difference reference seismogram shown in Figure 7.

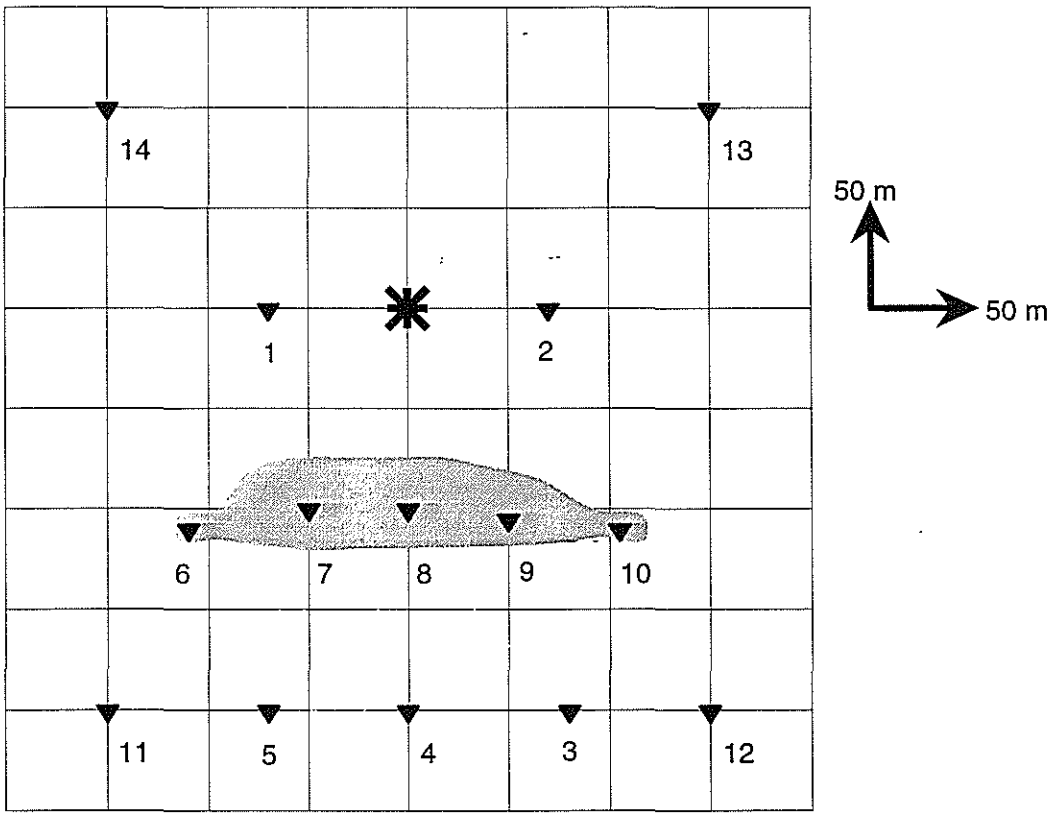

Figure 9: Locations of the source (star) and the receivers (triangles) used for comparison between the MMP and FD solutions as presented in Figure 10.

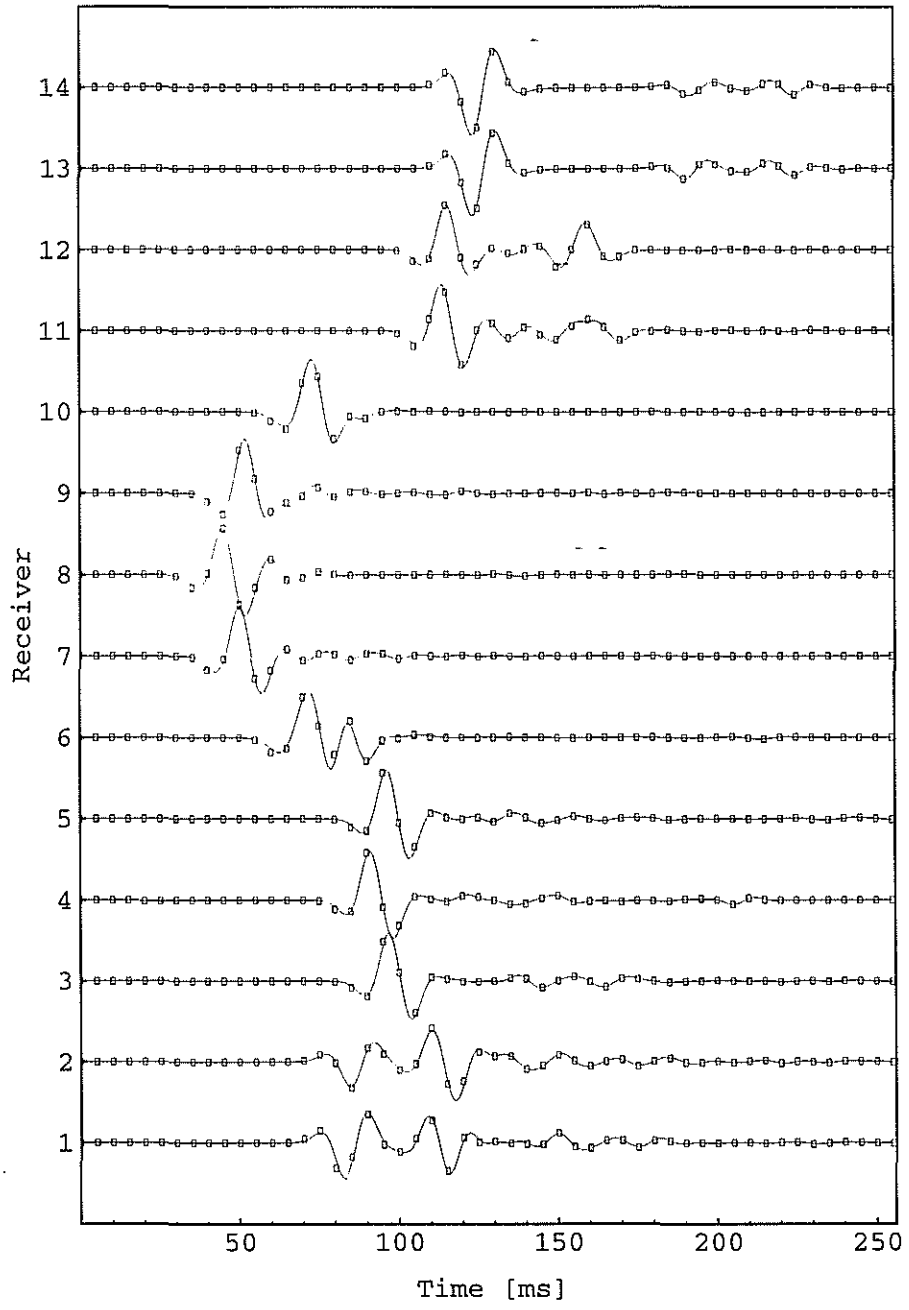

Figure 10: Comparison of the MMP solution (solid line) with the FD solution (boxed). The exact location of the receivers is given in Table (1) and Figure 9. Receivers 1, 2, 13 and 14 are above the scatterer; 6, 7, 8, 9, and 10 are in the scatterer; and 3, 4, 5, 11, and 12 are below the scatterer.

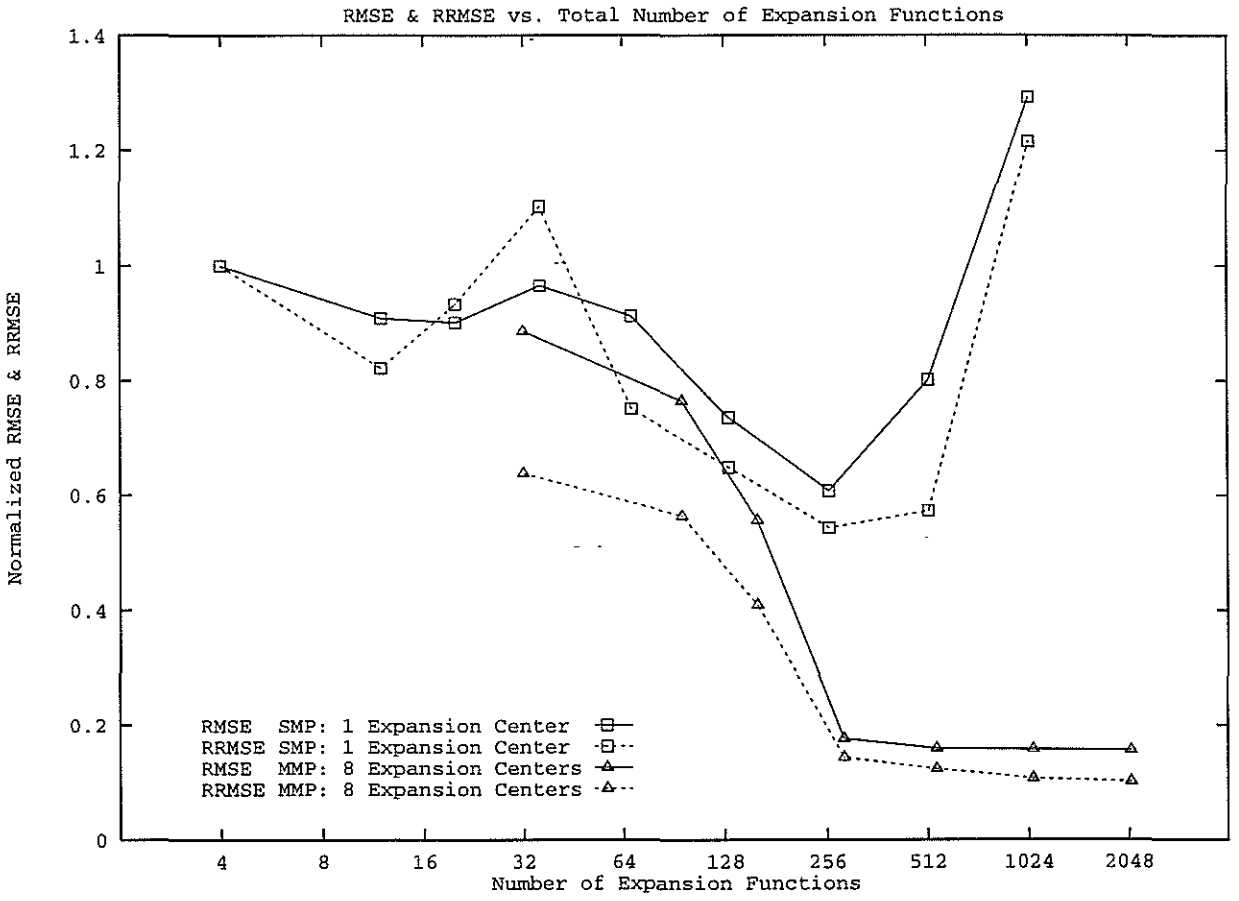

Figure 11: Comparison between the traditional eigenfunction expansion SMP (boxes) and the MMP expansion (triangles). Shown is how the total number of expansion functions affects the RMSE (solid) and RRMSE (dashed) compared to the FD reference solution. For 256 and more expansion functions, the MMP expansion converge. The SMP actually never converges since it violates the sampling condition for more than 256 expansion functions.

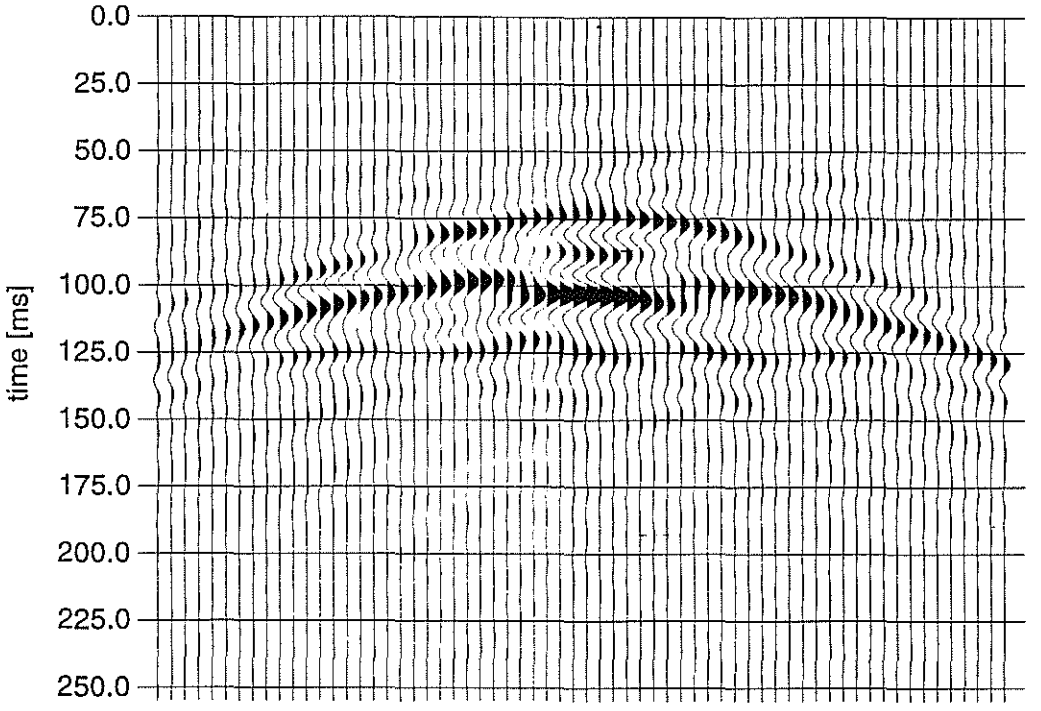

Figure 12: The seismogram for the case where 64 expansion functions are used. The seismogram is very noisy. Some of the prominent features in Figure 7 begin to show up, but the expansions have not yet converged. More terms have to be used to obtain convergence.

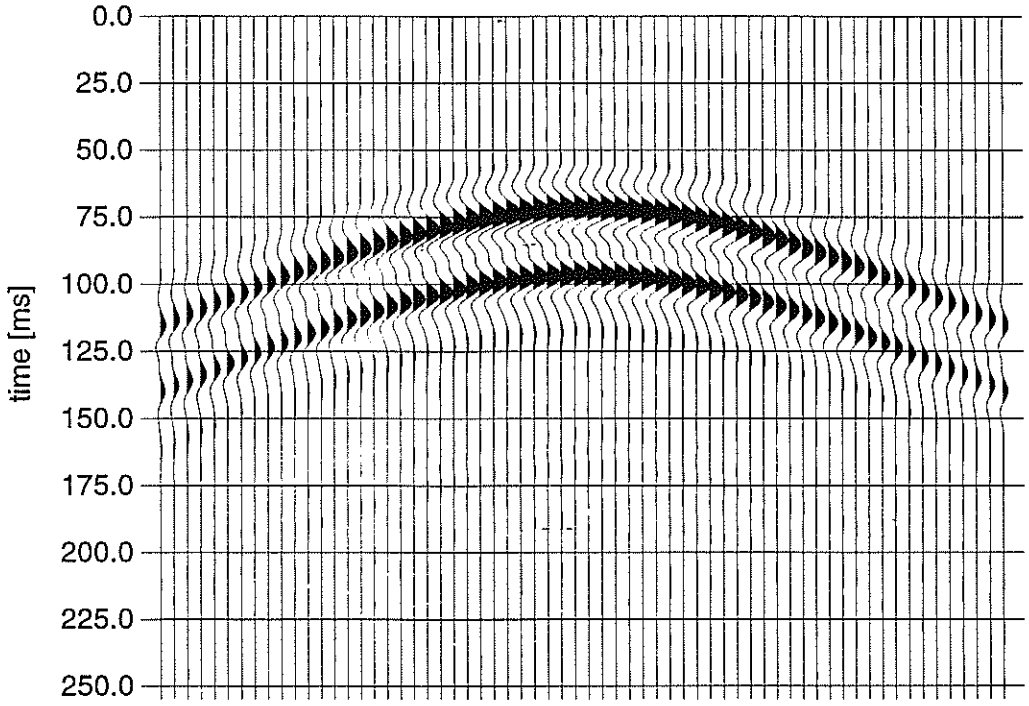

Figure 13: The seismogram for the case where only 4 expansion functions are used. Clearly, no self-interaction of the scattered wavefields is possible. Unfortunately, the seismogram is clean enough to be mistaken as correct.

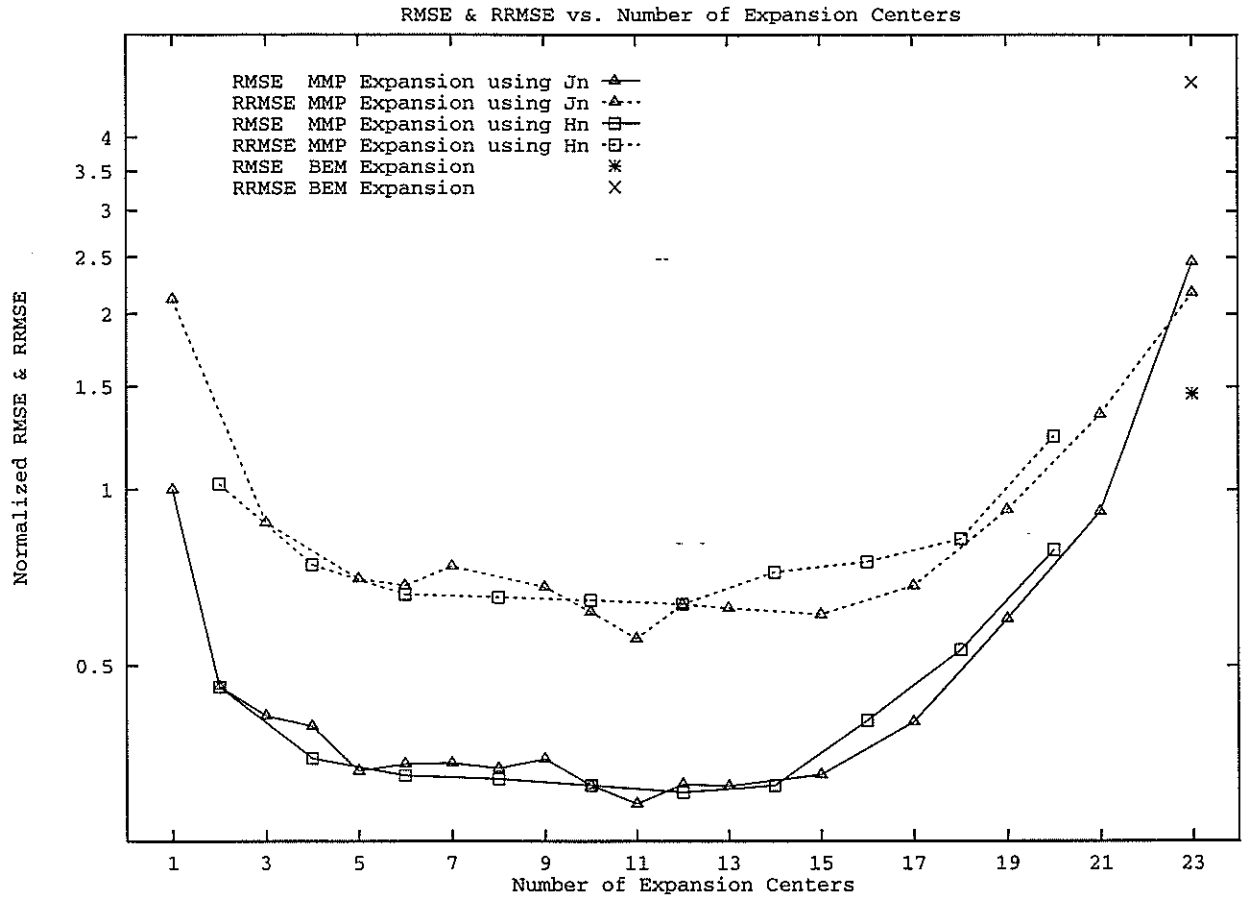

Figure 14: Effect of the number and location of expansion centers. The total number of expansion functions is kept constant at 256 while the number of expansion centers is varied from 1 up to 23. Expansions using the same expansion centers $\mathbf{x}_p^d \in \Gamma^1$ for $\phi^0, \psi^0, \phi^1, \psi^1$, and thus Bessel functions J_n, as well as expansions using expansion centers $\mathbf{x}_p^0 \in \Gamma^1$ for ϕ^0, ψ^0 and $\mathbf{x}_p^1 \in \Gamma^0$ for ϕ^1, ψ^1, and thus Hankel functions H_n, are tested. The difference between these two kinds of expansions is rather small. Placing all expansion centers onto the boundary and using only the terms of 0^{th} order corresponding to a simple boundary element expansions fails surprisingly.

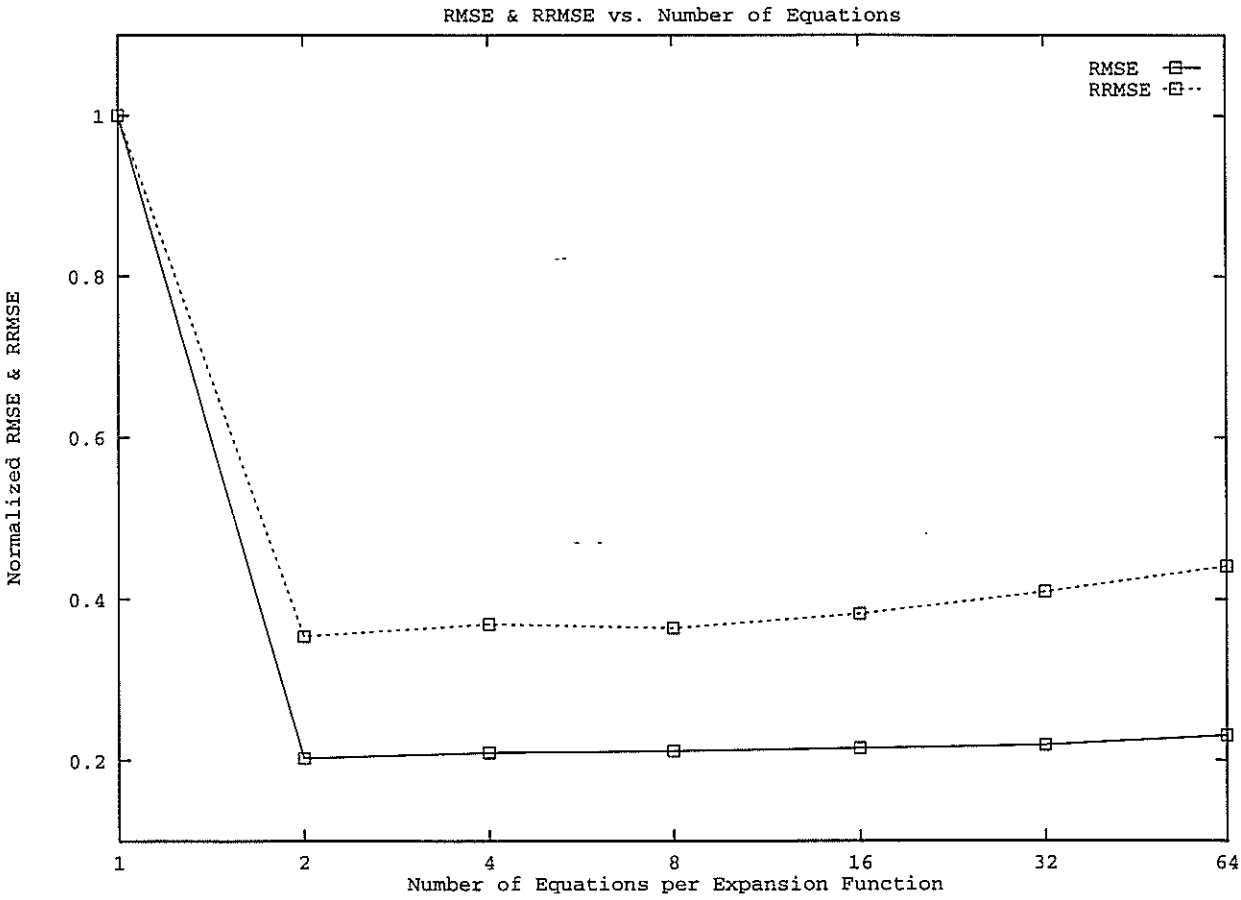

Figure 15: Influence of the number of matching points on the expansion with 256 expansion functions and 8 centers of expansion. Each matching point provides 4 equations. Since the expansion is non-orthogonal, using as many equations as unknowns to be resolved does not yield a correct result. Adding more and more equations to the system increases the condition number and thus the RMSE (solid) and RRMSE (dashed) are increased due to numerical errors.